AGU PUBLICATIONS

Water Resources Research

RESEARCH ARTICLE

10.1002/2013WR015177

Detection of spatially limited high-porosity layers using crosshole GPR signal analysis and full-waveform inversion

Anja Klotzsche[1], Jan van der Kruk[1], John Bradford[2], and Harry Vereecken[1]

[1]Agrosphere IBG-3, Forschungszentrum Jülich, Jülich, Germany, [2]Department of Geosciences, Boise State University, Boise, Idaho, USA

Key Points:

- High-contrast layers generate specific waveguide phenomena in crosshole GPR
- Novel amplitude analysis indicates discontinuous waveguide in GPR data
- High-resolution full-waveform inversion results are confirmed by porosity logs

Correspondence to:
A. Klotzsche,
a.klotzsche@fz-juelich.de

Citation:
Klotzsche, A., J. van der Kruk, J. Bradford, and H. Vereecken (2014), Detection of spatially limited high-porosity layers using crosshole GPR signal analysis and full-waveform inversion, *Water Resour. Res.*, *50*, 6966–6985, doi:10.1002/2013WR015177.

Received 17 DEC 2013
Accepted 15 JUL 2014
Accepted article online 17 JUL 2014
Published online 26 AUG 2014

Abstract High-permittivity layers, related to high-porosity layers or impermeable clay lenses, can act as low-velocity electromagnetic waveguides. Electromagnetic wave phenomena associated with these features are complicated, not well known and not easy to interpret in borehole GPR data. Recently, a novel amplitude analysis approach was developed that is able to detect continuous low-velocity waveguides and their boundaries between boreholes by using maximum and minimum positions of the trace energy profiles in measured GPR data. By analyzing waveguide models of different thickness, dip, extent, permittivity, and conductivity parameters, we extend the amplitude analysis to detect spatially limited or terminated waveguides. Waveguides that show high-amplitude elongated wave trains are most probably caused by a change in porosity rather than a change in clay content. In a crosshole GPR data set from the Boise Hydrogeophysical Research Site, two terminated wave-guiding structures were detected using the extended amplitude analysis. Information gained from the amplitude analysis improved the starting model for full-waveform inversion which imaged the lateral extent and thickness of terminated waveguides with high resolution. Synthetic data calculated using the inverted permittivity and conductivity models show similar amplitudes and phases, as observed in the measured data, which indicates the reliability of the obtained models. Neutron-Neutron logging data from three boreholes confirm the changes in porosity and indicate that these layers were high-porosity sand units within low-porosity, poorly sorted sand, and gravel units.

1. Introduction

Our ability to monitor hydrological processes and characterize subsurface properties is critical to developing a predictive and improved understanding of groundwater flow and contaminant transport. Most alluvial aquifers consist of heterogeneous sedimentary deposits showing a wide range of depositional structures and textures [*Koltermann and Gorelick*, 1996]. High-porosity layers, preferential flow paths, and impervious clay lenses are important for accurate modeling of groundwater flow and solute transport processes. Such heterogeneities within aquifers can be limited in thickness and lateral extent, such that detailed characterization of such small-scale, high-contrast layers is difficult.

Traditionally, hydrological parameters of aquifers are obtained by drilling (e.g., logging tools, core samples), and/or tracer and pumping tests. These methods provide either high vertical resolution (order of centimeters) close to the probes that suffers from a poor lateral resolution, or, they provide an averaged response over a large sample volume (e.g., pumping test). These methods are inadequate for detailed characterization of small-scale, high-contrast zones. A method that can provide both high resolution and lateral information is required.

Over the last decades, geophysical methods such as seismics, electrical resistivity tomography, and ground penetrating radar (GPR) have been widely applied and showed great potential to provide a detailed, minimally invasive characterization of hydrological relevant properties [e.g., *Doetsch et al.*, 2012; *Garambois et al.*, 2002; *Hubbard et al.*, 2001; *Hubbard and Rubin*, 2000; *Irving et al.*, 2009; *Mangel et al.*, 2012; *Topp et al.*, 1980]. The GPR method is able to provide two electromagnetic parameters at once, the relative dielectric permittivity ε_r, and the electrical conductivity σ, which influence the velocity and attenuation of the waves, respectively. The dielectric permittivity is mainly influenced by the porosity and pore structure. Because of the high contrast of permittivity in air $\varepsilon_r = 1$, and water approximately $\varepsilon_r \sim 80$, the permittivity is highly correlated with soil water content and for saturated conditions with porosity. For example, for dry sand $3 < \varepsilon_r < 5$, whereas for saturated sands $20 < \varepsilon_r < 30$ [*Davis and Annan*, 1989]. The electrical conductivity σ is influenced by porosity and other soil properties such as ion concentration, soil texture, and clay content.

In particular, crosshole (borehole to borehole) tomographic imaging using ground penetrating radar pulses is well suited to derive high-resolution images and to monitor infiltrations and recharge processes of aquifer systems [e.g., *al Hagrey and Müller*, 2000; *Alumbaugh et al*., 2002; *Ellefsen*, 1999; *Looms et al*., 2008; *Tronicke et al*., 1999; *Winship et al*., 2006]. Crosshole GPR uses high-frequency electromagnetic pulses that are emitted from a dipole-type antenna in a borehole. The transmitted and scattered electromagnetic waves are recorded in a second borehole by a receiver antenna. Dense ray-coverage between the boreholes is achieved by changing the positions of the transmitting and receiving antennas. The center frequency and dominant wavelengths of common borehole GPR antennas is in the range of 20–250 MHz and 0.4–5 m, respectively, for common geologic materials. For example, *Hubbard et al*. [1997] and *Binley et al*. [2001] used crosshole travel time GPR tomography to compare changes of the electromagnetic velocity before and after infiltration and mapped relative moisture changes. *Kowalsky et al*. [2005] applied a joint inversion of time-lapse GPR travel times and hydrological data to obtain soil hydraulic and dielectric parameters at the field scale, while *Looms et al*. [2008] used crosshole electrical resistivity tomography and GPR travel time tomography to monitor unsaturated flow and transport in an aquifer. *Dafflon et al*. [2011] jointly inverted several GPR crosshole planes to characterize the porosity of an alluvial aquifer near Boise, Idaho, USA.

Small-scale heterogeneities related to preferential flow paths or clay lenses within aquifers are often characterized by a high ε_r contrast with the surrounding medium, and can be limited in thickness and lateral extent. High-contrast layers caused by an increase in porosity (high water content and permittivity) or clay content (high permittivity and conductivity), act as a low-velocity waveguide when the thickness of the layer is smaller than the in situ dominant wavelength of the GPR signal [*Arcone et al*., 2003; *van der Kruk et al*., 2010, 2009]. The electromagnetic wave speed increases outside of these layers because of the decrease in dielectric permittivity. Beyond the critical incidence angle, the waves are totally reflected within the waveguide at the layer boundaries and multiple reflections with late arrivals occur, forming trapped elongated wave trains that may propagate over large distances. The presence of deeper waveguides between two or more boreholes was studied for seismic data [e.g., *Franssens et al*., 1985; *Greenhalgh et al*., 2007], but the number of studies for borehole GPR data are limited [e.g., *Ellefsen*, 1999]. The wave phenomena that occur in the presence of a low-velocity waveguide between two boreholes are complicated, not well known and not easy to interpret; consequently, they are often not identified or ignored.

Crosshole GPR data are traditionally inverted by applying ray-based methods that use first-arrival times and first-cycle amplitudes of each signal. The inversion minimizes the misfit between measured and simulated data. Smoothing and damping constraints are normally applied to stabilize the inversion, but this comes at the cost of the resolution. Further, the resolution of these techniques is limited because only a small amount of the data is exploited and layers smaller than the dominant wavelength cannot be resolved. High-amplitude and late arrival events such as those caused by a waveguide are ignored and not incorporated in the inversion. Over the last decade a new imaging method, full-waveform inversion (FWI) was developed to exploit the full information content of the data. This method significantly improves the resolution of the subsurface, and can provide both ε_r and σ images at decimeter-scale [*Ernst et al*., 2007a, 2007b; *Meles et al*., 2011, 2010; *Klotzsche et al*., 2010]. Our FWI algorithm is based on a 2-D finite difference time domain (FDTD) solution of Maxwell's Equations and simultaneously updates the permittivity and conductivity. Nevertheless, full-waveform inversion is computationally expensive and an accurate but smoothed starting model that yields synthetic data within half a wavelength of the measured data is necessary to obtain reliable inversion results.

Recently, full-waveform inversion of experimental crosshole data enabled the identification and characterization of a low-velocity gravel aquifer waveguide between two boreholes [*Klotzsche et al*., 2012, 2013] that was related to changes in porosity and indicated zones of preferential flow. For a transmitter located within the waveguide and receivers straddling the waveguide depth range, trapped electromagnetic waves with anomalously high-amplitudes and late arrival elongated wave trains (at least one order of magnitude higher trace amplitudes) could be observed. For the receiver positions within the waveguide, a distinct minimum in the trace energy was visible when the transmitter was located outside the waveguide. These observations formed the basis of an amplitude analysis that explores these positions where maxima and minima of the trace energy profiles (squared amplitude of each trace) occur. This method was able to identify laterally continuous low-velocity waveguides and their boundaries from the measured data only [*Klotzsche et al*., 2013]. However, full-waveform inversion and the combined interpretation of the permittivity and conductivity remain necessary for the detailed characterization of the waveguide, especially in case of lateral heterogeneity.

In this paper, we extend this imaging method to detect and identify high-porosity layers that are spatially limited or terminated between the boreholes. Since the wave phenomena are not well understood, we perform a detailed synthetic study to improve our understanding of the observed wave phenomena. The investigation of spatially limited and terminated waveguides enables the extension of the amplitude analysis such that heterogeneous waveguides with limited lateral extent can also be identified and characterized. We investigate the benefits and limitations of the method by investigating different relevant hydrological structures with varying the thickness, the extension, the orientation, and the model parameters (ε_r and σ) of low-velocity waveguides present between two boreholes. We apply our extended amplitude analysis and the full-waveform inversion to an experimental crosshole GPR data set acquired at the Boise Hydrogeophysical Research Site (BHRS), which contains two heterogeneous low-velocity waveguides with limited lateral extent. The starting models of the full-waveform inversion are improved by using the information gained by the amplitude analysis, and the final full-waveform inversion results showed a very good fit in shape, phase, and amplitude.

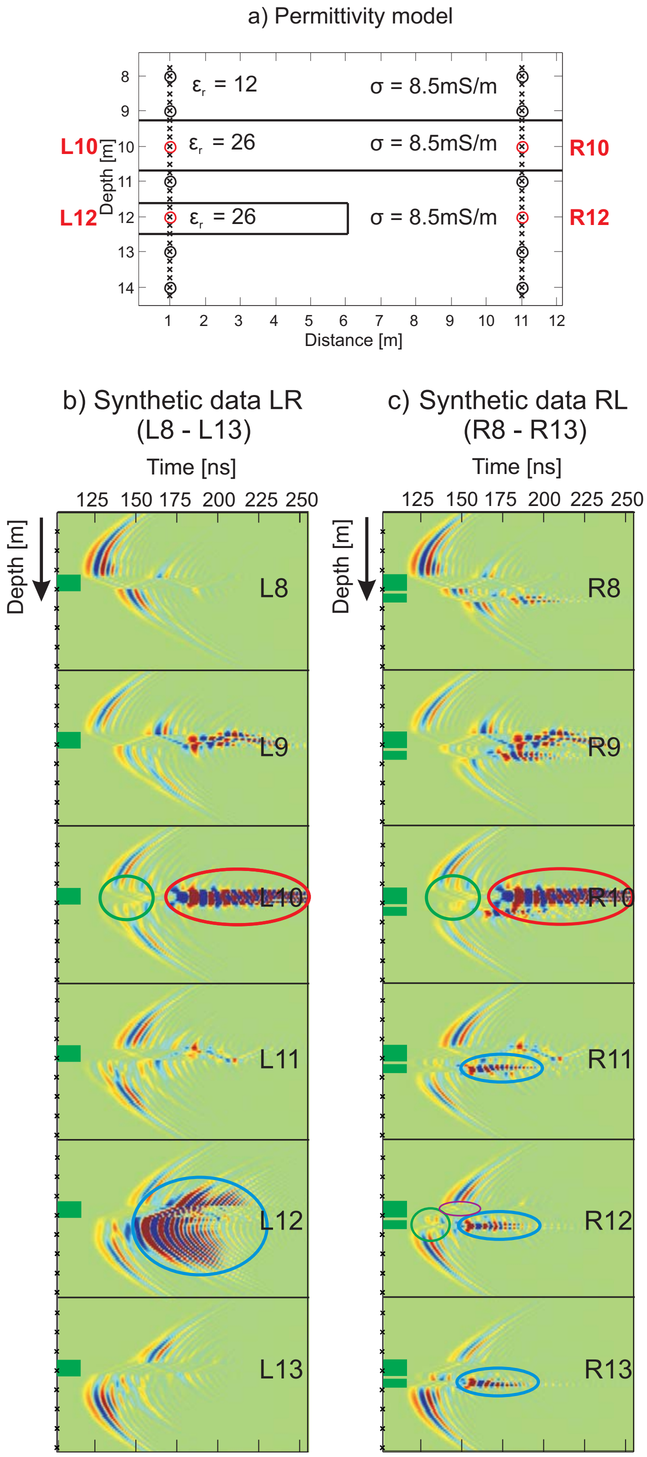

Figure 1. (a) Permittivity model used for generating synthetic data. The two layers are waveguides with a higher-permittivity value than the surrounding medium. (b) Synthetic data for transmitters L8–L13, with L10 and L12 located within the waveguides. (c) Synthetic data for transmitter R8–R13, with R10 located within a waveguide layer. The green boxes indicate the position of the waveguides. L10 and R10 data show elongated wave trains with high amplitudes at later arrivals and a reduced velocity indicated by the red circles, whereas the events caused by the second terminated waveguide (reduced lateral extension) are marked by blue circles. Every tenth receiver position is marked with a black cross, starting at receiver position 10.

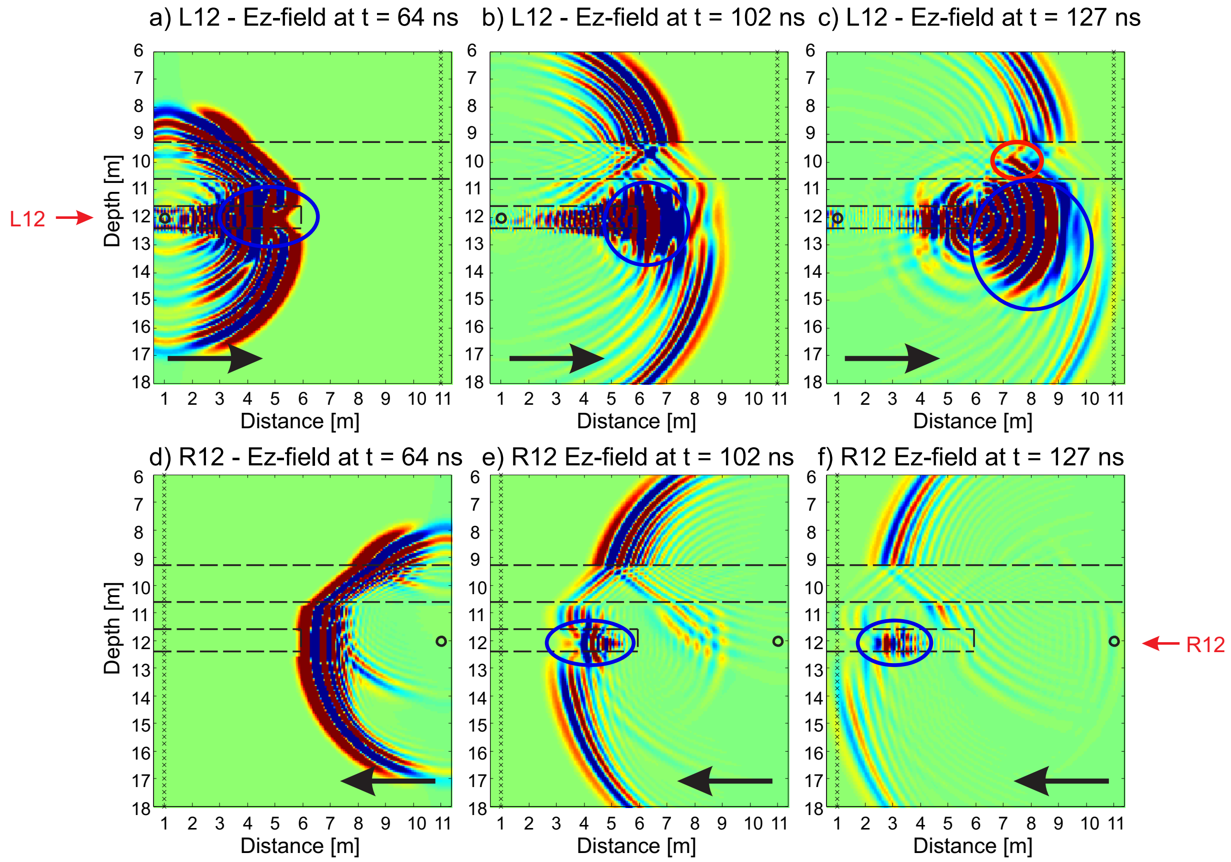

Figure 2. Forward modeled snapshots of the electrical field distribution for transmitter L12 and R12 of the synthetic model shown in Figure 1a, whereas the black dashed lines indicate the waveguide at (a) 64 ns, (b) 107 ns, and (c) 127 ns. The transmitter and receiver positions are indicated by the black circles and crosses, respectively. The blue and red circles indicate events that are discussed in the text.

2. Synthetic Models of Continuous and Terminated Low-Velocity Waveguides With Limited Lateral Extend

For the synthetic study, we use high relative permittivity (low-velocity) waveguide layers with $\varepsilon_r = 26$ present within a background medium with relative permittivity of $\varepsilon_r = 12$, similar to previously inverted experimental data of a gravel aquifer [e.g., *Klotzsche et al.*, 2012]. The conductivity is $\sigma = 8.5$ mS/m for the entire domain. We use a semireciprocal (transmitter and receiver can be reversed) measurement setup with 21 transmitter and 81 receiver positions with a vertical spacing of 1 m and 0.25 m, respectively. By interchanging transmitter and receiver boreholes, the acquisition plane is measured from left to right and from right to left and referred to as LR and RL, respectively. The transmitters are numbered for the left and the right borehole from top to bottom with L1–L21 and R1–R21 starting at 1 m depth until 21 m depth.

Calculating the critical angle θ_C

$$\theta_C = \sin^{-1}\left(\sqrt{\frac{\varepsilon_2}{\varepsilon_1}}\right) \tag{1}$$

with ε_1 and ε_2 as the relative permittivities of the waveguide and the surrounding medium, respectively, we obtain for our synthetic model a $\theta_C \geq 42.8°$ for which total internal reflection occurs. The synthetic models are calculated using a 2-D FDTD algorithm to obtain corresponding synthetic radar data.

First, we applied a synthetic model that contains both a continuous and a terminated waveguide with limited lateral extent (Figure 1). For the L10 and R10 transmitters (every tenth receiver position is indicated by a black cross), which are located in the continuous waveguide layer, clearly elongated wave trains and high-amplitude late arrivals in the synthetic data are detected over the depth range of the low-velocity waveguide, which cause the peak maxima in the trace energy profiles. The symmetry in the observations indicates a continuous waveguide layer. For L9 and R9 elongated wave trains are visible showing smaller amplitudes than L10 and R10. In contrast, the data for the terminated waveguide layer show a clear asymmetry: R12 again indicates elongated wave trains with increased amplitudes for the terminated layer, whereas the data for L12 shows a spreading of higher amplitudes at later arrivals. These amplitudes are smaller than for the continuous waveguide.

To investigate the high-amplitude spreading over many receivers for the L12 transmitter, we plot snapshots at 64, 102, and 127 ns of the vertical electrical wavefield (Ez) for transmitter L12 in Figures 2a–2c, respectively. At earlier times (Figure 2a), most energy is trapped within the terminated waveguide at 12 m depth, as evidenced by the elongated wave train caused by internal multiple reflections beyond the critical angle of $\theta_C = 42.8^\circ$. In addition, a delayed travel time can be observed caused by the reduced velocity (see blue circle). At 102 ns (Figure 2b), the wavefield starts to leave the waveguide, the trapped energy is released, and the bundled energy then spreads into the homogeneous half space with amplitudes higher than the other wavefronts. This behavior continues also at 127 ns where the wavefield is more spread (see blue circle) and reaches the receivers on the right side. In contrast, the emitted wave from R12 is more equally distributed until 64 ns (Figure 2d). When it encounters the waveguide (shown in Figures 2e and 2f) some energy is trapped within the waveguide, which results in an elongated wave train with a delayed travel time (blue circles), but with a smaller amplitude than for the continuous waveguide.

In the continuous waveguide at 10 m depth, the wavefield transmitted into the waveguide from below is refracted toward the vertical, and then refracted away from vertical after being transmitted out of the waveguide. In this area, the angle of incidence is below the critical angle and both transmission and reflection can occur. Since the wave speed above and below the waveguide is faster than within the waveguide, two interfering head waves, from above and below the waveguide can be identified at 127 ns (Figure 2c, red circle). We can also clearly see how the amplitude is minimized by this interference (indicated by the red circle) which causes a minimum in the measured trace energy as can be observed in Figure 1 indicated by the purple circle at Transmitter position R12.

3. Waveguide Detection Using Amplitude Analysis

Klotzsche et al. [2013] introduced an amplitude analysis approach to identify and detect horizontally continuous wave-guiding structures. We extend this analysis to lateral terminated waveguides based on the above modeling observations following these steps:

1. The data of each measurement plane are scanned for transmitter positions that show significant late arrival high-amplitude elongated wave trains. These wave trains and high amplitudes indicate the presence of a low-velocity waveguide.

2. For the transmitters of step 1, the corresponding trace energy (summation of the squared amplitude) for all receiver positions are calculated and receivers that have one or two orders of magnitude higher energy levels at certain depth intervals compared to receivers located outside of these ranges are identified. For these transmitter positions, a distinct maxima peak in the trace energy can be picked.

3. The trace energy is calculated for all the other transmitter positions (except the transmitters of steps 1 and 2). Generally, for transmitters outside of a waveguide region, intermediate amplitudes are detected for most of the receiver positions in the opposite borehole, whereas for the receivers straddling a waveguide zone, significantly diminished amplitudes and a minimum in trace can be observed in the depth region around the previously found maxima in energy.

4. The minima in the trace energy distributions for each of the transmitter positions are selected when the energy is at least one or two orders of magnitude lower than for the maxima positions of step 2.

5. The obtained maxima and minima positions are plotted at the corresponding receiver depths; the maxima are within the waveguide layer and the minima indicate with increasing distance of the transmitter to the waveguide the upper and lower boundaries of the waveguides.

6. High-amplitude elongated wave trains identified for transmitters in both boreholes at similar depths (similar to Figure 1 for L10 and R10) indicate a continuous waveguide between the two boreholes.

7. High-amplitude elongated wave trains that are detected for only one borehole, and spread late arrival high amplitudes that can be identified on the opposite borehole, as shown in Figure 1 for R11–R13 and L12, respectively, indicate the presence of a terminated waveguide having a limited lateral extent (see Figure 1a).

With increasing length of a terminated waveguide between two boreholes, the vertical spreading of the high amplitudes decreases until elongated wave trains can be observed in both boreholes, as in the case of a continuous waveguide. In contrast, when the length decreases, the spreading of the high amplitudes will increase and lower amplitudes will be sensed by the receivers. Consequently, the spreading of the high amplitudes allows a qualitative estimate of how far the waveguide extends between the boreholes. For a quantitative high-resolution distribution estimation of the medium properties, the full-waveform inversion is still necessary.

3.1. Amplitude Analysis for Different Synthetic Models

Because of depositional processes, the porosity of aquifers can vary strongly and can greatly influence fluid flow and transport processes. Therefore, we chose six synthetic models I–VI with different thicknesses, layering, dipping, and extent of one or two low-velocity (high-porosity) waveguides (Figure 3a) that represent different hydrogeological structures and sequences that can occur in aquifers. The observed maxima and minima positions in the trace energy profiles for the LR and RL transmitter positions are shown in Figures 3b–3e. The picked maxima and minima positions from the LR and RL trace energy distributions are shown in Figures 3f and 3g by red and green crosses as function of receiver depth.

The waveguide layer in model I (first row of Figure 3) has a thickness of 1 m (equal to the transmitter spacing) and represents a continuous high-permittivity layer that can be associate with a high-porosity zone. *Klotzsche et al*. [2013] were able to resolve similar structures with a permittivity of 20–26 that were identified as high-porosity zones and indicated that such layers can be related to zones of preferential flow. For each of the semireciprocal setups, one transmitter L10 and R10 is located within this layer, marked by the thick black circle. For both of these transmitters, a distinct maximum in the trace energy profile is observed at 10 m depth, having at least a magnitude 3 times higher than a transmitter located outside of this zone. For all the transmitter positions located outside the waveguide, a distinct minimum in the trace energy is visible for receivers present within the waveguide layer. Moreover, a plateau of minimum values is present which indicates the thickness of the waveguide. The trace energy profiles for planes LR and RL are identical because of the symmetric waveguide spanning between the boreholes. By plotting the picked maxima and minima positions from the trace energy profiles against receiver depth (Figures 3f and 3g), we see that picked minima positions represent the boundaries of the waveguide.

Because small-scale high-contrast structures can vary strongly in the thickness and can be limited in vertical extension, we combine in synthetic model II (second row of Figure 3) two high-porosity waveguide layers with a decreased and increased thickness of 0.5 and 2 m, respectively. For the first layer with the decreased thickness, a similar behavior of the trace energy profiles to model I is observed and we detect one maxima position at 10 m depth. However, the spatial sampling of the receivers of 0.25 cm is too sparse to precisely define the boundaries of the thin waveguide using the picked minima positions of the amplitude analysis. Consequently, the depth localization depends on the spatial sampling of the receiving antenna and the boundaries can only be positioned at measurement points. In contrast, when two transmitter positions are located in a waveguide with a thickness of 2 m, two maxima in the trace energy profiles occur. For each of the profiles, clear minima in a certain range spanning the thickness of the waveguide are visible. The picked minima positions precisely identify the boundaries of the waveguide, when transmitter positions with a larger distance from the waveguide are used. For other models (not shown) with increasing thickness of the layer, more transmitter positions with a larger distance to the waveguide are necessary to precisely estimate the waveguide boundaries.

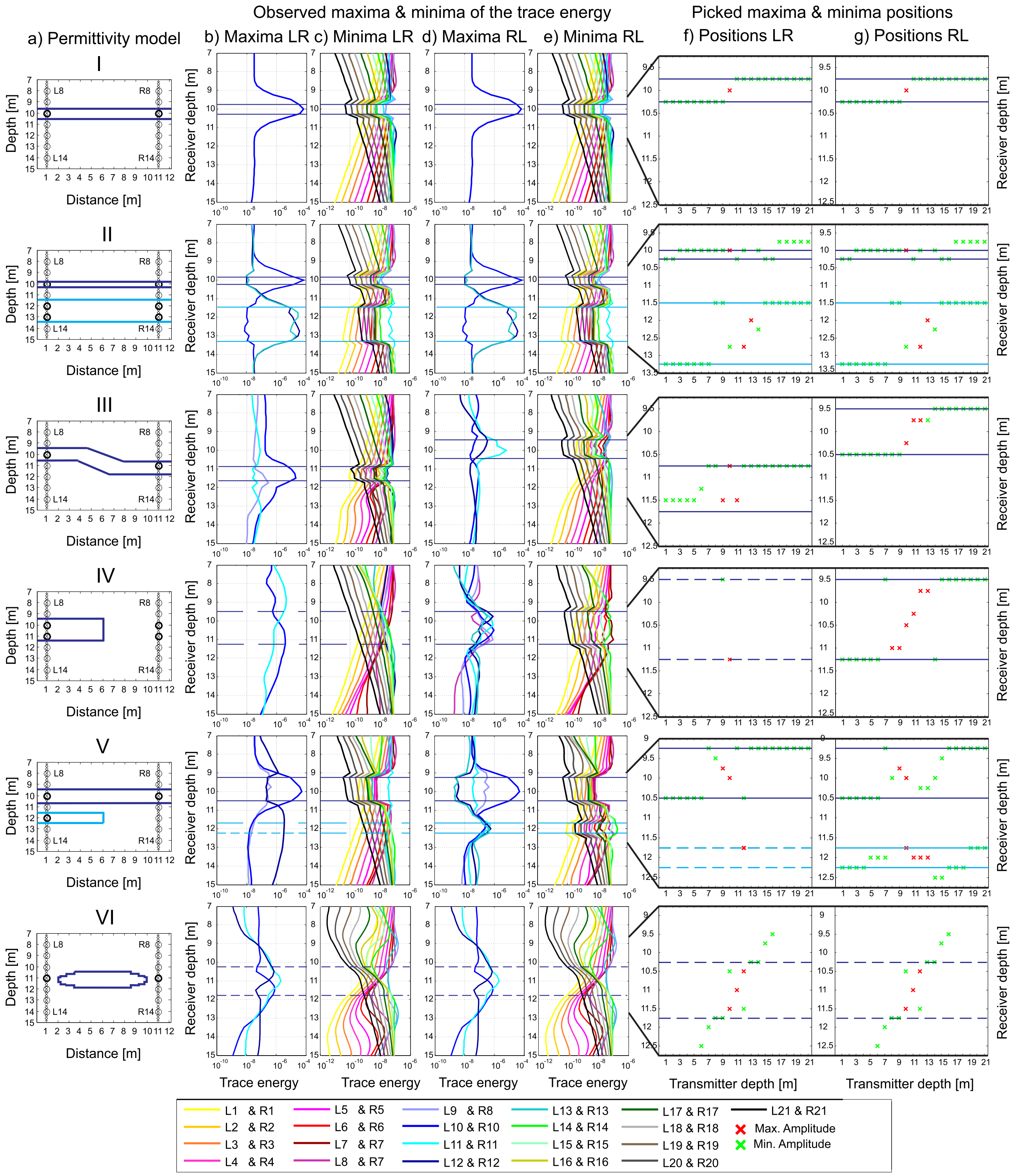

Figure 3. (a) Synthetic permittivity models I–VI. (b–e) Maxima and minima of trace energy profiles for the semireciprocal measurement setups LR and RL. Note, that the maxima and minima traces have a different *x* axis range and each transmitter has a certain color affiliation. (f) LR and (g) RL picked positions of the maxima (red crosses) and minima (green crosses) of the trace energy for each transmitter along receiver depth. The blue lines indicate the waveguide boundaries close to the corresponding borehole in which the receivers are located.

Stratigraphic layering is influenced by deposition and geological processes, therefore high-contrast layers can tend to have a dip. In the case of a dipping waveguide in model III, the amplitude analysis identifies the waveguide and detects the boundaries at both sides of the waveguide. Picking the maxima positions is more challenging and the trace energy is reduced compared to a nondipping waveguide (approximately 1 order of magnitude). Here the dip of the layer has a large influence on the angle of the critically reflected waves within the waveguide such that energy which was critically reflected before is now transmitted and less energy is trapped. With increasing angle of the dipping layer, less energy is trapped in the waveguide and more energy is released in the surrounding medium.

Next, we want to analyze if high-permittivity (high porosity) structures can be identified that are not continuously horizontally layered. Such layers are normally related to changes in material and texture, rather than zones of preferential flow. Model IV is a terminated waveguide with a limited lateral extent where no clear maxima or minima can be identified in the LR profiles for either of the transmitters located within the waveguide. As indicated by the wave propagation shown in Figures 1 and 2, the difference in energy is less than one magnitude. For the RL plane, we observe six maxima in the trace energy profiles (one magnitude higher than the minima profiles) for receivers straddling the waveguide depth. Using the picked maxima and minima positions, the boundaries of the waveguide close to the left borehole can again be identified. The minima plateaus of the plane RL indicate the thickness of the layer. In the next synthetic model V, we combine a horizontal continuous layer and a terminated waveguide (see also Figures 1 and 2). Similar to models I and IV, where only one transmitter is located inside the waveguide, the boundaries of the waveguide layers can be obtained using the extended amplitude analysis approach.

In the last synthetic model VI, we defined a lens of high-permittivity (high-porosity) material that is spatially limited in that it is not connected to either of the boreholes. We observe in this case for three transmitters at each side a maxima in the trace energy. However, the picking of the minima is more difficult and only minima are selected if the difference between the maxima and minima is more than one order of magnitude. In contrast to model IV, we are able to select some minima positions even when the waveguide is not connected to the borehole, which is probably caused by smaller distance between the borehole and the waveguide layer. However, the minima positions do not line up and therefore the thickness of the lens cannot be estimated. Note that no clear minima plateaus are visible, which is probably caused by the spreading of the wave as soon as it leaves the low-velocity layer (similar to Figures 1 and 2). Similar results were obtained for rectangular structures of the same size as for the used lens.

In summary, when a high-porosity waveguide is continuous between the boreholes similar wavefields with clear, high-amplitude elongated wave trains are present for receivers in both boreholes at similar depths. When a terminated or dipping waveguide is present, a semireciprocal measurement setup [see *Oberröhrmann et al.*, 2013] is necessary to check whether high-amplitude spreading in the data occurs or if a second elongated wave train is present at a different depth. For a high-porosity waveguide lens that is not connected to both boreholes, the corresponding spreading of the wave can be used to detect a waveguide and maxima positions can be observed when the distance from the lens to the borehole is not too large. However, precise identification of the boundaries is not possible. Also as the separation of the boreholes gets larger the spreading effect becomes less pronounced and the detection of the waveguides may not be possible.

3.2. Influence of Permittivity and Conductivity on Waveguide Behavior

Here, we test the influence of higher and lower-permittivity and conductivity values of the waveguide. In theory, a low-velocity waveguide can be caused by either an increase of porosity in saturated media (high permittivity) or of clay content (high conductivity and high permittivity). It is not clear if the increased attenuation caused by the higher conductivity of clay can compensate the high amplitudes that can be observed in the presence of a low-velocity waveguide. Therefore, we use a synthetic model with a waveguide of 2 m thickness (Figure 4a), where two transmitters for each of the semireciprocal measurements are located inside the waveguide.

First, we vary the relative permittivity of the waveguide layer using $\varepsilon_{r1} = 26$ (similar to Figures 1–3), $\varepsilon_{r2} = 30$ for a slightly increased porosity, and $\varepsilon_{r3} = 20$ for a slightly decreased porosity, with a homogeneous conductivity of $\sigma = 8.5$ mS/m. The critical angles are given by θ_{C1} ($\varepsilon_{r1} = 26$) = 42.8°, θ_{C2} ($\varepsilon_{r2} = 30$) = 39.2°, and θ_{C3} ($\varepsilon_{r3} = 20$) = 50.8°. As expected, the trace energy for the two transmitters L10 and L11 increases with increasing permittivity within the waveguide because of the decreased critical angle which traps more energy within the waveguide (Figure 4b). Consequently, higher permittivity causes larger maximum trace energy and corresponding maxima are more distinct and easier to pick.

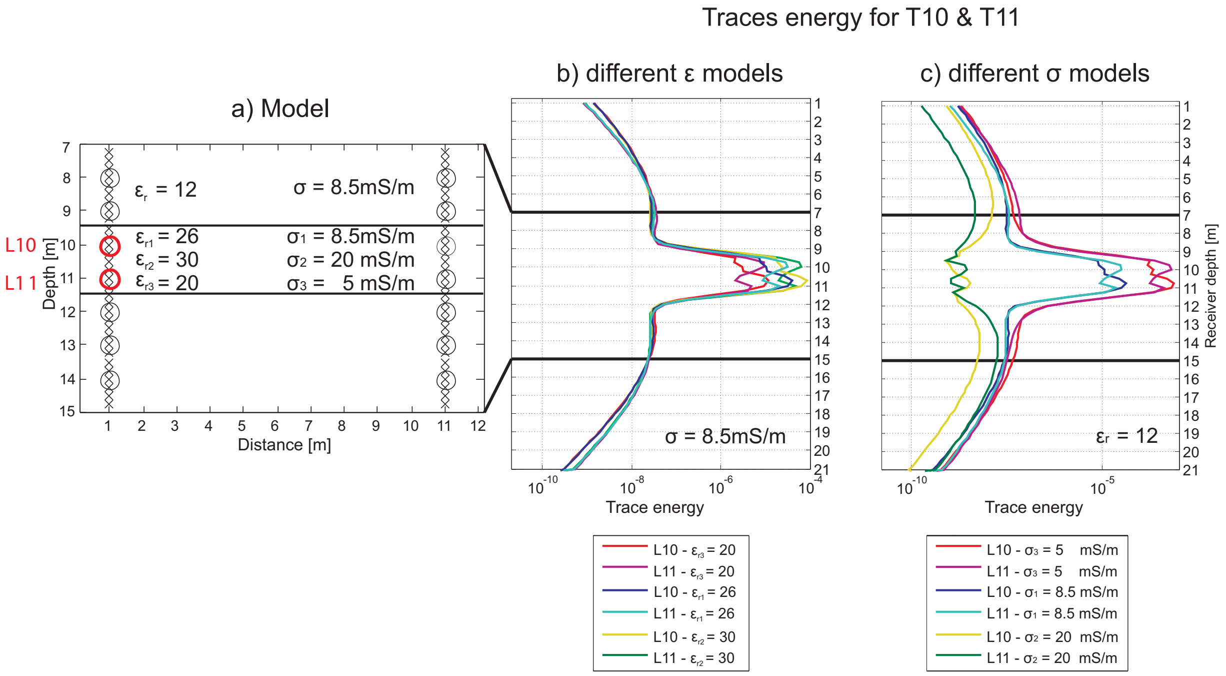

Figure 4. (a) Permittivity and conductivity models used for generating synthetic data. (b) Comparison of the T10 and T11 trace energy profiles (both located in the waveguide) for different ε_r values for the waveguide and $\sigma = 8.5$ mS/m. (c) Comparison of the trace energy profiles for T10 and T11 for varying σ for the waveguide and $\varepsilon_r = 26$.

Second, we define three synthetic models using different conductivity values for the waveguide layer: $\sigma_1 = 8.5$ mS/m (homogeneous space), $\sigma_2 = 20$ mS/m (possible value for a sand rich clay layer) and $\sigma_3 = 5$ mS/m, while the permittivity is constant in the layer with $\varepsilon_r = 26$ ($\theta_C = 42.8°$). In the case of a higher conductivity (Figure 4c, green lines) no maximum in the trace energy for transmitters located in the waveguide is observed because of the conductivity-induced attenuation. In contrast, for a smaller conductivity (Figure 4c, red lines) higher trace energy is detected. Additionally, in all cases distinct minimum positions and corresponding minimum plateaus in the trace energy are observed for the transmitter located outside the waveguide (not shown). Therefore, if trace energy forms a distinct maximum, which is at least one order of magnitude higher than for transmitters outside the waveguide, in the presence of elongated wave trains, the waveguide is caused by a change in porosity or soil water content. In contrast, when no elongated wave trains and no distinct maxima occur in the trace energy profiles, but instead diminished minima positions and minima plateaus are present, the waveguide is probably caused by a change in clay content.

4. Experimental Study: Boise Hydrogeophysical Research Site

We applied the extended amplitude analysis and full-waveform inversion to an experimental data set acquired at the Boise Hydrogeophysical Research Site (BHRS). The site is located 15 km from Boise, Idaho, USA, and is close to the Boise River. During the last two decades, several studies were carried out using different methods to characterize the aquifer [*Barrash and Reboulet*, 2004; *Barrash et al*., 2006; *Bradford*, 2010; *Clement and Barrash*, 2006; *Clement et al*., 1999; *Dafflon et al*., 2011; *Mwenifumbo et al*., 2009; *Oldenborger et al*., 2007; *Straface et al*., 2011; *Tronicke et al*., 2004]. The unconfined aquifer comprises an 18–20 m thick layer of heterogeneous coarse cobble-sand fluvial deposits. It is underlain by a red clay aquitard. *Barrash and Clemo* [2002] subdivided the aquifer into five hydrostratigraphic units primarily by using porosity differences: four cobble-dominated units and one sand unit (see Figure 5c and Table 1).

4.1. Data Acquisition

A set of 13 boreholes are arranged in a semirandom distribution of conceding rings within a diameter of 20 m (Figures 5a and 5b). The crosshole GPR data set was provided by the Department of Geosciences of the Boise State University for the SEG-AGU Hydrogeophysics workshop 2012 (www.seg.org/events/

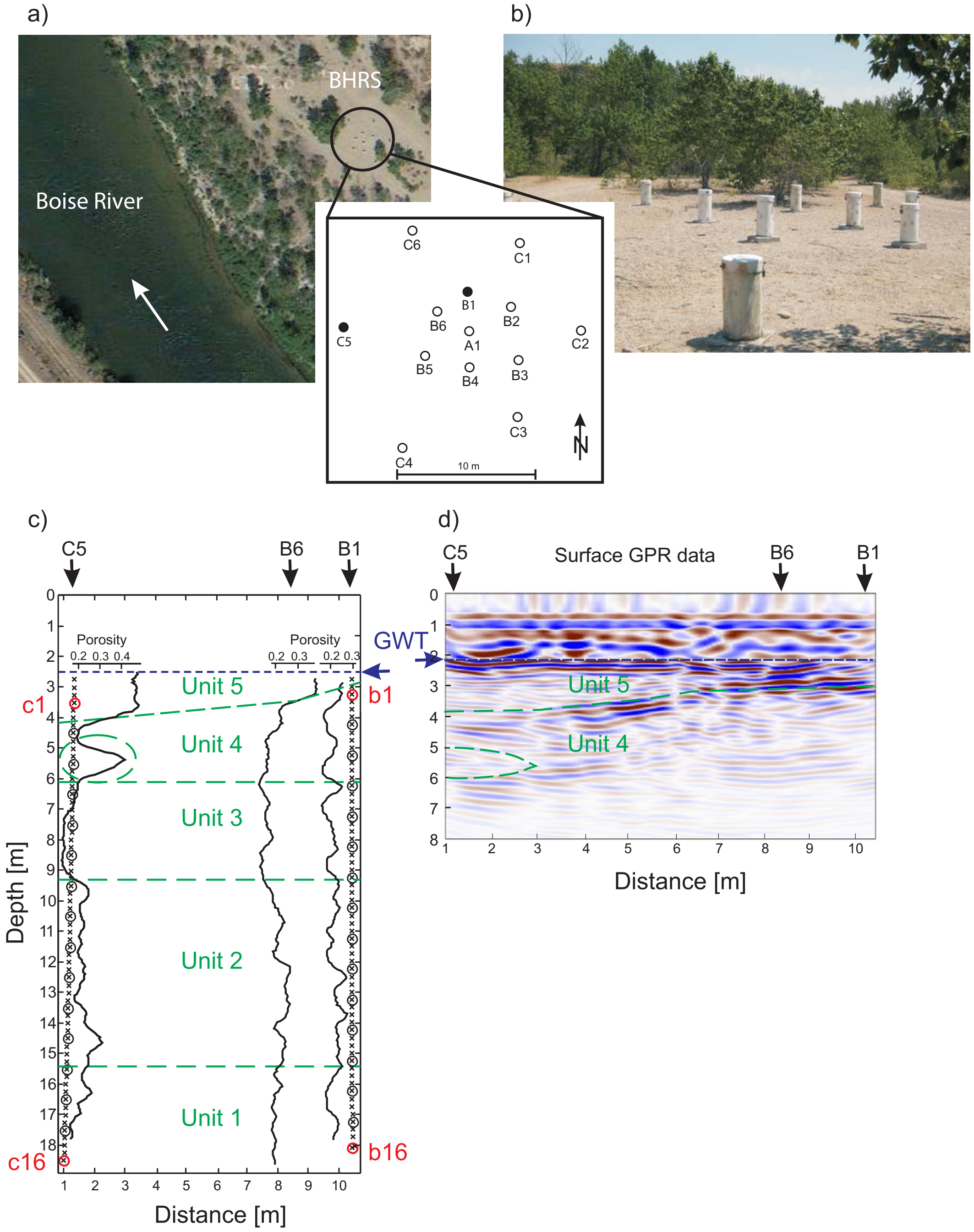

Figure 5. (a) Overview of the BHRS showing the location of the boreholes close to the Boise River. The white arrow indicates the flow of the river. The GPR cross borehole measurements were performed in the two black marked boreholes C5 and B1 (modified from Google Maps). (b) Picture of the test site. (c) Schematic setup of the investigation area between C5 and B1 where the transmitter and receiver positions are shown with circles and crosses, respectively. Neutron porosity logs measured in wells C5, B6, and B1 are shown in black. (d) Migrated surface GPR data acquired between C5 and B1 using a 200 MHz antenna. The groundwater table (GWT) is marked in blue and in green are the different units obtained by *Barrash and Clemo* [2002], which can vary in depth over the entire test site.

upcoming-seg-meetings/hydrogeo2012). The data were acquired in October 2011 using the Sensors and Software pulseEKKO Pro system with 100 MHz antennas in the boreholes C5 and B1, which are approximately 10 m apart and slightly tilted (indicated in Figure 5c). A semireciprocal crosshole GPR geometry was used (Figure 5c), with 16 transmitter positions and 64 receiver positions in each borehole below the groundwater table, which was at approximately 2.5 m depth. The vertical spacing of the transmitter and receiver positions is 1 m and 0.25 m, respectively, and for each position the coordinates were obtained by a

Table 1. Mean Porosity Values and Dominate Compositions of the Five Hydrostratigraphic Units of All Wells Located in the Central Part at the BHRS Estimated From Core and Neutron-Neutron Porosity Logs [*Bradford et al.*, 2009]

Unit	Approximate Thickness (m)	Mean Porosity (%)	Porosity Variance (%)	Dominant Composition
5	0–4	42.9	0.3	Coarse sand
4	1–5	23.3	0.2	Pebble/cobble dominated
3	3	17.2	0.06	Pebble/cobble dominated
2	6	24.3	0.2	Pebble/cobble dominated
1	2	18.2	0.06	Pebble/cobble dominated
All	18–20	25.2	0.4	

deviation log. In the following, we introduce the notation convention for the transmitter positions in boreholes C5 and B1, where the positions are numbered from c1 to c16 and b1 to b16, respectively. The transmitter c1 and b1 are located close to the groundwater table at 3.5 m and 3.2 m depth, respectively. For comparison, a surface GPR reflection profile was acquired with a pulseEKKO Pro system with 200 MHz antennas directly between the wells C5 and B1 (Figure 5d). This profile was acquired at a different date than the borehole measurements; therefore, the groundwater table differs. The GPR profile was depth migrated using a simplified three layered velocity model obtained by common-midpoint measurements along that profile. The depth of the stratigraphic boundary between Units 4 and 5, as estimated by the GPR profile and the Neutron porosity logs of C5, B6, and B1 (black graphs in Figure 5c) are similar. The porosity log of C5 also indicated a high-porosity zone between 5 and 6 m depth, which is suggested in the surface data.

4.2. Waveguide Detection Using Extended Amplitude Analysis

High-amplitude late arrival elongated wave trains occur in the data of transmitters c1–c3 and b1–b3, which are present directly below the water table (Figures 6a and 6b). Wave-guiding structure I is identified directly below the water table for both sides of the measurements in the data of transmitters c1, b1, and b2, as indicated by the red circles. For these three transmitters, we clearly observe high-amplitude late arrival elongated wave trains, which are more spread out for the c1 data. This asymmetry indicates that the waveguide is not continuous and does not extend laterally to borehole B1. Wave-guiding structure II is indicated by the blue circles between 5 and 6 m depth, which have lower amplitudes and are more spread out for c2 and c3 compared to b2 and b3. Moreover, a distinct velocity reduction is indicated by the green circles and can be observed for the b2 and b3 transmitters. Again a clear asymmetry is present which indicates that wave-guiding structure II has also a reduced lateral extent and is not continuous in between the two boreholes. These observations are very similar to the observations for the synthetic studies IV and V (see Figure 3), where a waveguide was present with a truncated extent.

The picked maxima and minima positions of the trace energy profiles in the depth range where the high-amplitude elongated wave trains were identified are shown in Figures 7a–7c and 7d–7f for the C5–B1 and B1–C5 planes, respectively. Two clear maxima can be observed for transmitter gathers c1 and c3 (red crosses in Figure 7a). The minima positions indicated (green crosses in Figure 7b) are less clear and difficult to pick around the picked maximum at about 3.5 m depth (one order of magnitude smaller that the maxima). The minima positions around the picked maximum at 5.3 m are not very pronounced, but allow easy picking. Because of the location of both wave-guiding structures close to the water table, there are no transmitter positions above the layers to define the boundaries of the wave-guiding structures in more detail. Also, the picking of the maxima and minima is more challenging caused by the less pronounced maxima and minima positions in the profiles.

Using the picked maxima and minima positions along the receiver depth, we identify the boundaries of the wave-guiding structures close to borehole B1 (black lines in Figure 7c). For plane B1–C5 also clear maxima can be identified (Figure 7d). Moreover, very distinct minima positions in the trace energy profiles can be observed, especially between 5 and 6 m depth, which enables better identification of the waveguide boundaries (Figure 7f). The clearer minima and the reduced velocities that can be observed when the transmitters are located in borehole B1 both indicate that the waveguide is present at borehole C5, whereas it is not present anymore at borehole B1.

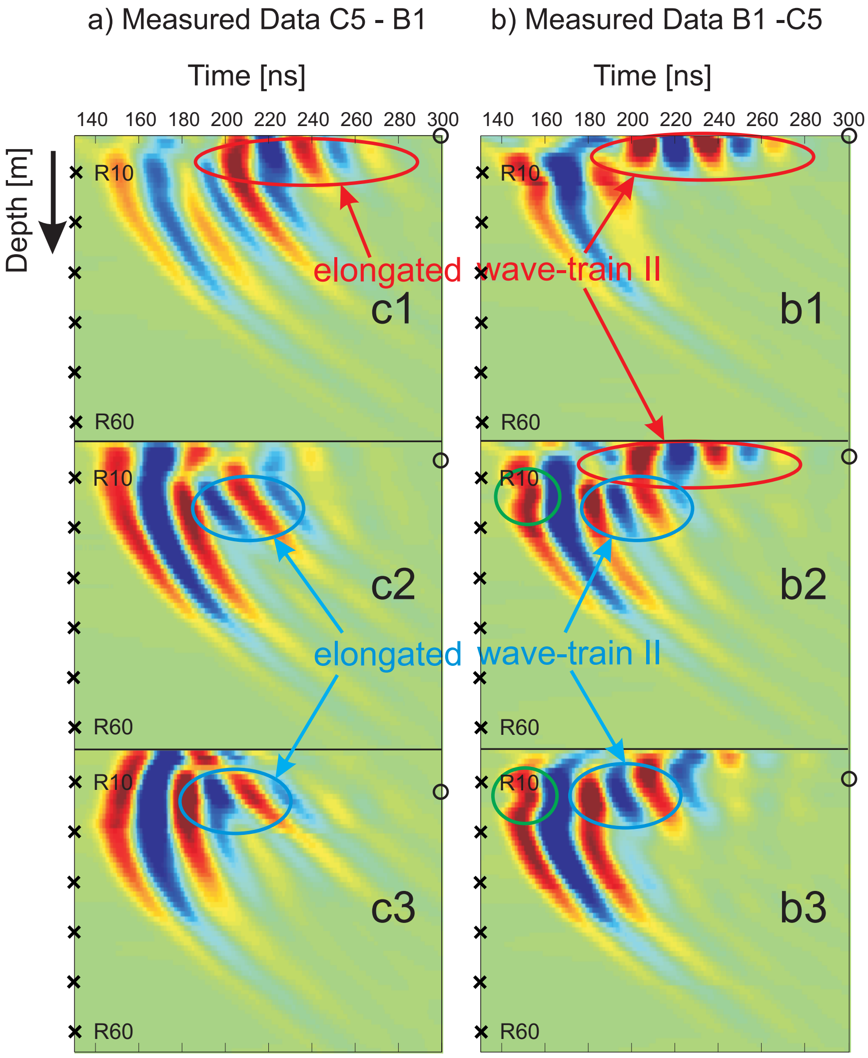

Figure 6. Recorded profiles for transmitters (a) c1–c3 and (b) b1–b3. The position of the transmitter is indicated by the black circle, whereas c1 and b1 are located close to the water table at 3.5 and 3.2 m depth, respectively. Every tenth receiver position is marked with black crosses (e.g., R10). The phenomena indicating wave-guiding structures are marked by red and blue circles. The reduced velocity in combination with the high-amplitude elongated wave train II are indicated in green. For both images, the same amplitude scale is used and the true amplitudes are shown, where high and low amplitudes are indicated by red and blue color, respectively.

4.3. Full-Waveform Inversion

To determine the lateral extent of the two wave-guiding zones, we performed the full-waveform inversion of the data that provides high-resolution images of the aquifer. We obtain starting models for the full-waveform inversion by performing a ray-based travel time and first-cycle amplitude inversion (Figures 8a and 8b). The permittivity model shows a smoothed intermediate permittivity layer, which is embedded between lower-permittivity layers. Because of the small range of conductivity we chose a homogeneous conductivity starting model for the full-waveform inversion with 8.5 mS/m, which represents the mean value of the first-cycle amplitude inversion. The estimated effective source wavelet, shown in the corner of Figure 8b, was obtained by using the starting models and following the full-waveform inversion approach based on a conjugate gradient updating discussed in *Klotzsche et al*. [2010]. In the ε_r and σ full-waveform inversion results that used the ray-based starting model (Figures 8c and 8d), the three main layers, obtained by the travel time inversion (see Figures 8a and 8b), are resolved with a higher-resolution and the root-mean-squared (RMS) error is reduced to 61.4% compared to the ray-based results (100%). Below 18 m depth in the σ tomogram (Figure 8d), the underlying clay is indicated by higher σ values. Still a significant misfit between the measured data for the c1, c2, b1, and b2 transmitters can be observed in

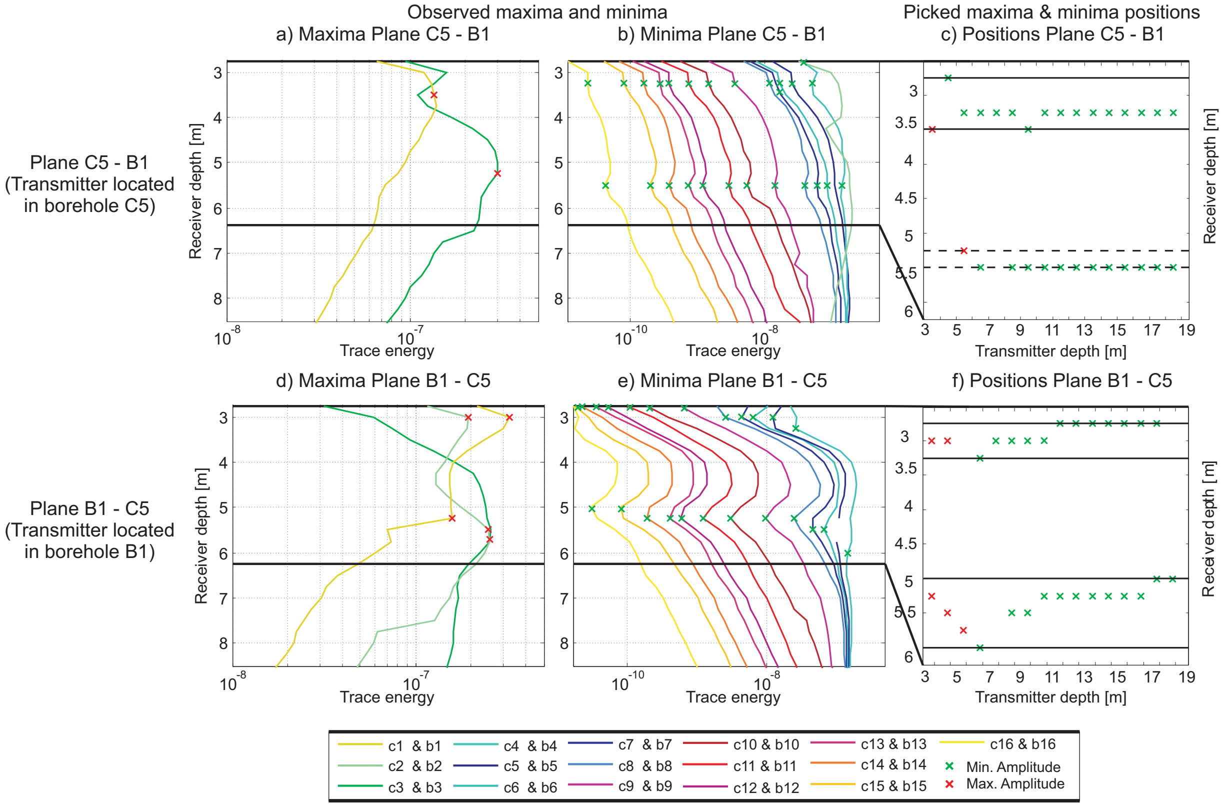

Figure 7. (a and d) maxima and (b and e) minima of trace energy profiles of the measured data and picked positions for the planes (c) C5–B1 and (f) B1–C5. The red and green crosses indicate the position of the maxima and minima of the energy, respectively. Each transmitter has a certain color affiliation. The black lines indicate the estimated waveguide boundaries using the amplitude analysis close to the corresponding borehole B1 and C5, respectively.

Figures 9a and 9d close to the water table (see red circles) and a remaining gradient can be observed (not shown, see *Yang et al*. [2013]). This indicates that the starting model close to the water table obtained by the ray-based inversion is not reliable, probably because of the low ray-coverage close to the water table (and the bottom of the inversion domain). The synthetic data calculated for the starting model have less overlap than half a wavelength with the measured data, such that cycle skipping occurred and the full-waveform inversion did not converge to the correct model [*Meles et al*., 2011; *Virieux and Operto*, 2009].

The information gained from the extended amplitude analysis, which indicates the presence of two discontinuous wave-guiding structures close to the water table, is now incorporated into the starting model by assuming a homogeneous higher permittivity ($\varepsilon_r = 17$) layer between the water table and 4 m depth. In this way, the starting model yields synthetic data that overlaps the measured data within half the dominant wavelength such that a convergence toward the global minimum is possible. The RMS error between the measured and modeled data, using the updated ε_r starting model, is reduced to 45.5% and a very good fit in shape, phase and amplitude is visible in Figures 9a, 9d, and 9c and 9f, respectively, for both acquisition planes. The good agreement includes the high-amplitude late arrivals caused by the two waveguides (see transmitter c1–c3 and b1–b3), which indicates the reliability of the obtained model.

The final ε_r and σ full-waveform inversion results (Figures 8e and 8f) show a high-permittivity waveguide layer with a thickness of about 1 m present between the water table, and 4 m depth. The layer extends from well C5 up to one meter before well B1 and then disappears. A high ε_r layer between 5 and 6 m depth is also present close to borehole C5, extends for about 3 m toward B1 and then disappears. The wave-guiding structures and boundaries obtained by the amplitude analysis (see Figure 7 and green boxes in Figure 8e) are confirmed by the full-waveform inversion result, including indications that the waveguides start at borehole C5, but do not extend to borehole B1. Whereas the amplitude analysis is not able to determine the lateral extent of the two waveguides, the full-waveform inversion exploits all information present in the

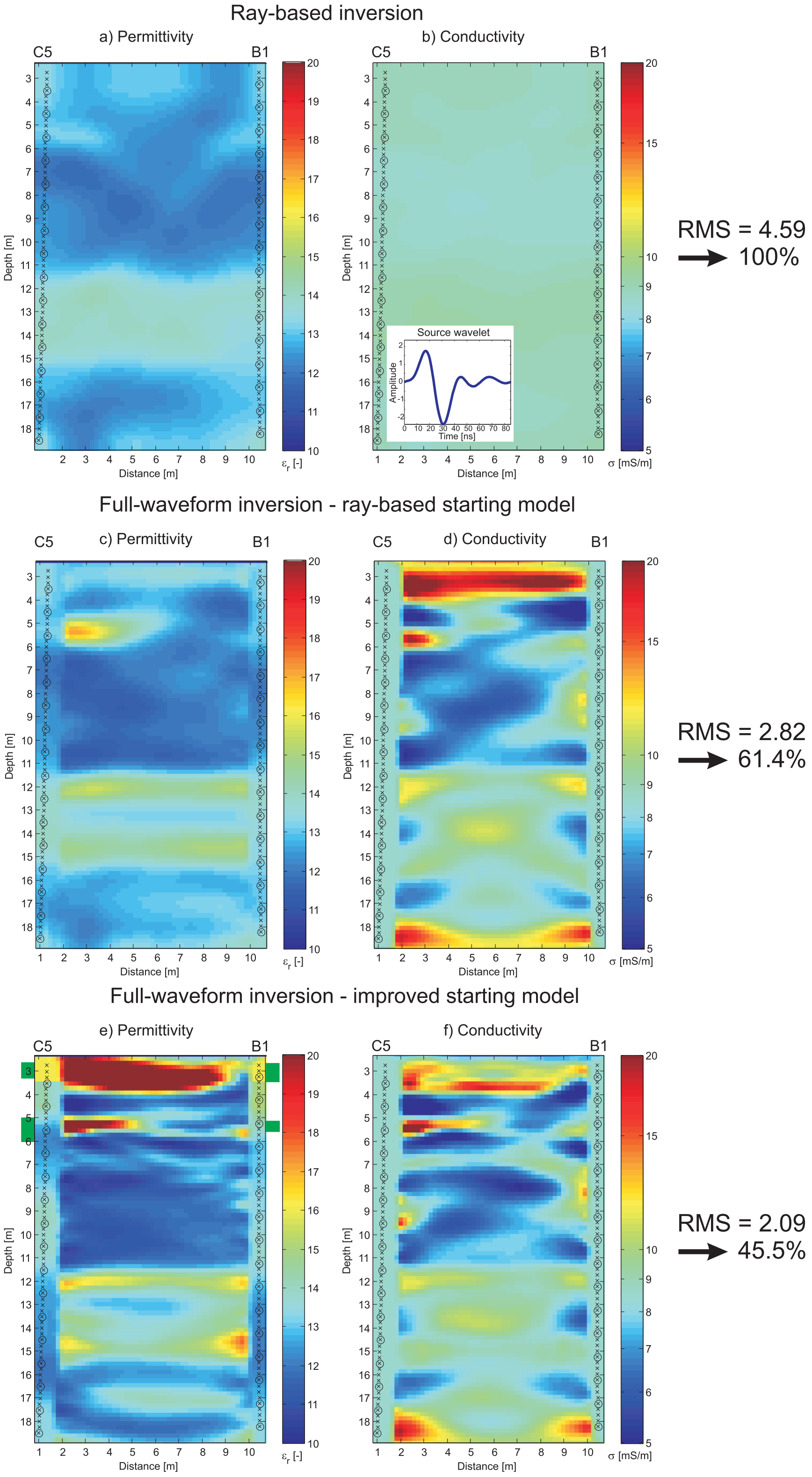

Figure 8. Ray-based (a) permittivity and (b) conductivity models obtained by the travel time and first-cycle amplitude inversion, respectively. Transmitter and receiver positions are marked with circles and crosses, respectively. Inset in Figure 8b shows the estimated effective source wavelet. (c) Permittivity and (d) conductivity results estimated by the full-waveform inversion using the ray-based starting models as shown in Figures 8a and 8b, respectively. (e) Final permittivity and (f) conductivity models obtained by the full-waveform inversion using the improved starting models. The green boxes on the left and right side of Figure 8e indicate the boundaries of the wave-guiding structures obtained from the amplitude analysis.

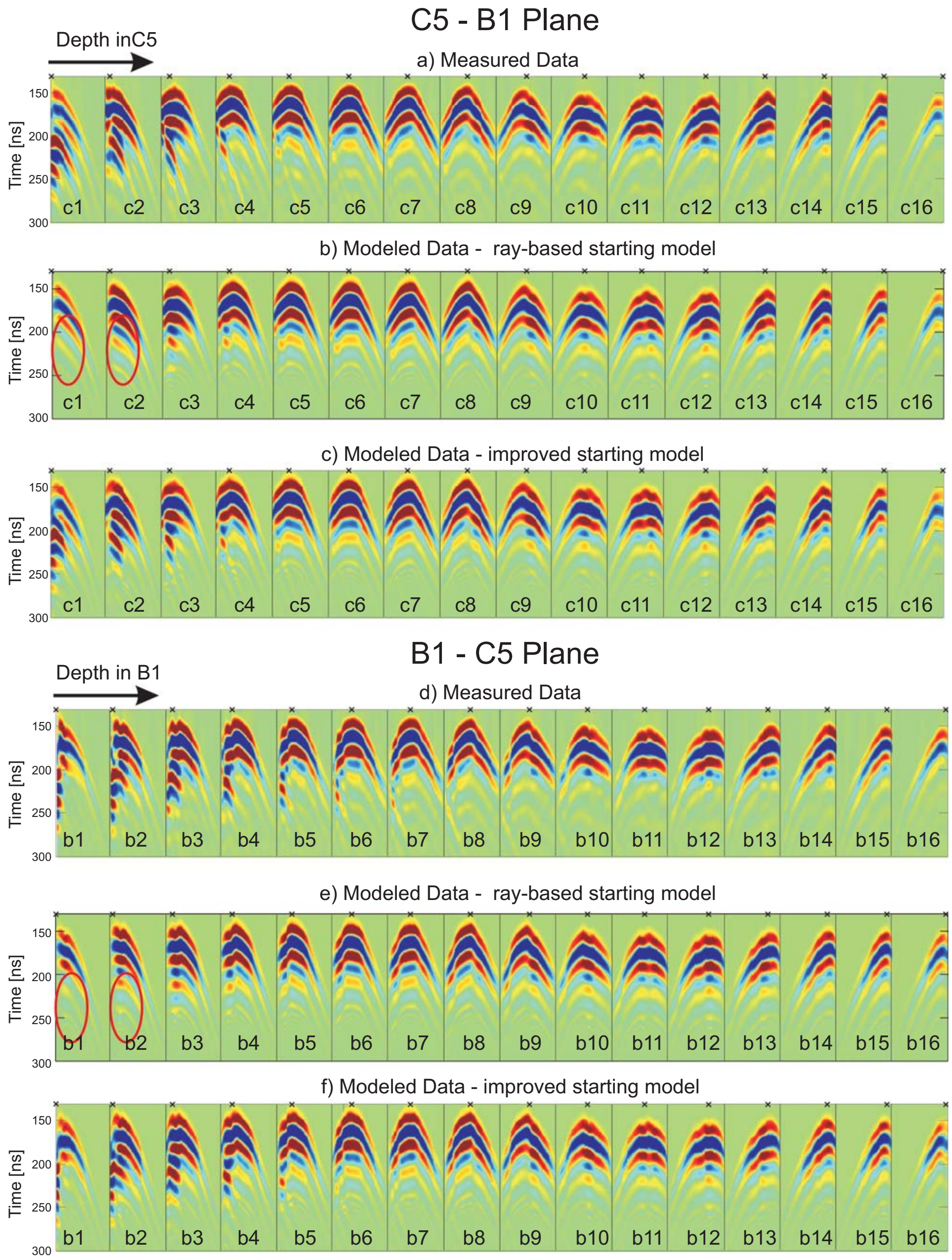

Figure 9. (a and d) measured data, (b and e) full-waveform modeled data using the ray-based starting model, and (c and f) full-waveform modeled data using the improved starting model for the planes C5–B1 (transmitters located in C5) and B1–C5 (transmitters located in B1). The images show true amplitudes with positive and negative amplitudes in red and blue, respectively. The black crosses illustrate the transmitter position.

measured data and images the waveguides with high resolution. The two wave-guiding layers are not identified by the ray-based approach (see Figures 8a and 8b) because it ignores the late time high-amplitude arrivals.

We investigated the wave propagation within the waveguide by forward modeling transmitters c1 and b1 using the final ε_r and σ full-waveform inversion results, similar to that shown in Figure 2. Within the snapshots of the vertical electrical wavefield of c1 and b1 at time 76 ns (Figures 10a and 10d), most of the radiated energy is trapped between 2.5 and 4 m depth, whereas for c1 a clear velocity reduction below 4 m depth is visible indicating the waveguide boundary, which is less clear close to borehole B1. At 102 ns (Figures 10b and 10e), the wavefield is trapped in both cases. At time 127 ns, the wavefield emitted from c1

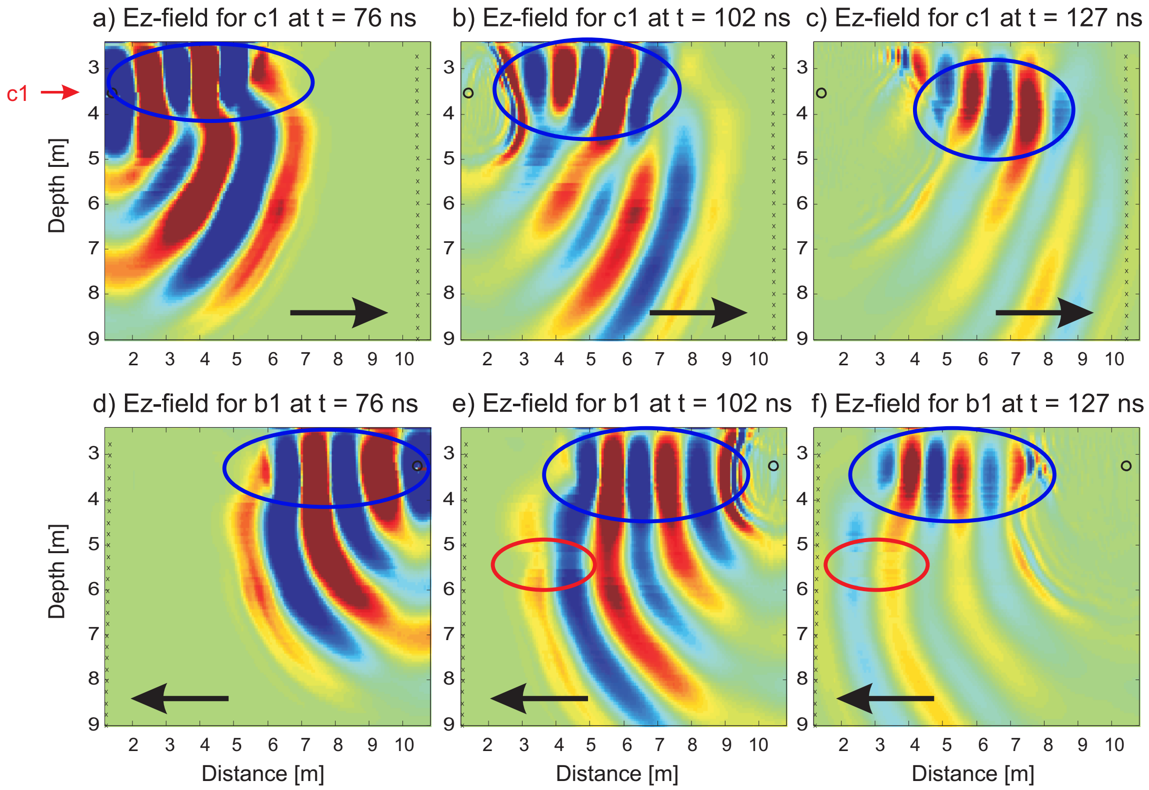

Figure 10. Forward modeled snapshots of the electrical field distribution for transmitter (a–c) c1 and (d–f) b1 for different time steps. The transmitter c1 and b1 positions are indicated by the black circle. The blue and red circles indicate events caused by the two different waveguides layers.

(see Figure 10c) starts to spread because it is no longer trapped in the waveguide. Therefore, a reduced maximum in the trace energy occurs (similar to the synthetic examples in Figure 2). The wavefield emitted from b1 (see Figure 10f) is still trapped in the waveguide and has formed an elongated wave train with less spread and a clear maxima in the trace energy (similar as the synthetic studies in Figure 2).

4.4. Comparison of the Full-Waveform Inversion Results and Logging Data

We validate the waveform inversion results and the findings of the energy analysis by comparing the results to Neutron-Neutron porosity logs acquired in wells C5 and B1 (see Figure 11). We converted the final waveform ε_r results into porosities Φ using the two-component CRIM equation [*Clement and Barrash*, 2006] for a saturated aquifer. Solving for porosity, the CRIM equation gives

$$\Phi = \frac{\sqrt{\varepsilon} - \sqrt{\varepsilon_S}}{\sqrt{\varepsilon_W} - \sqrt{\varepsilon_S}} \tag{2}$$

where ε_W and ε_S are the permittivity of water and the sediment, respectively. Here, we used $\varepsilon_W = 80.36$ and $\varepsilon_S = 4.6$ similar to *Clement and Barrash* [2006]. Additional porosity logging data are available for borehole B6 (see Figure 5), which is located close to the acquisition plane. For the full-waveform inversion porosity values of C5, B1, and B6, we use the mean of three cells next to the borehole (red graphs). The result from the waveform inversion corresponds well with all the logging data, especially in the upper part outlining the different thicknesses of the high-porosity/permittivity zone 5.

The logging data follows the trend of the high-porosity zones from the full-waveform inversion, indicating that the wave-guiding layer between 2.5 and 4 m depth is more pronounced close to well C5, is still present in well B6, but almost absent in B1 (see purple circles). The second waveguide zone is only indicated in well C5, and absent in well B1 and B6. Consequently, this zone vanishes between well C5 and B6 (see dashed black lines in C5 and B6). These layers are caused by a change of low

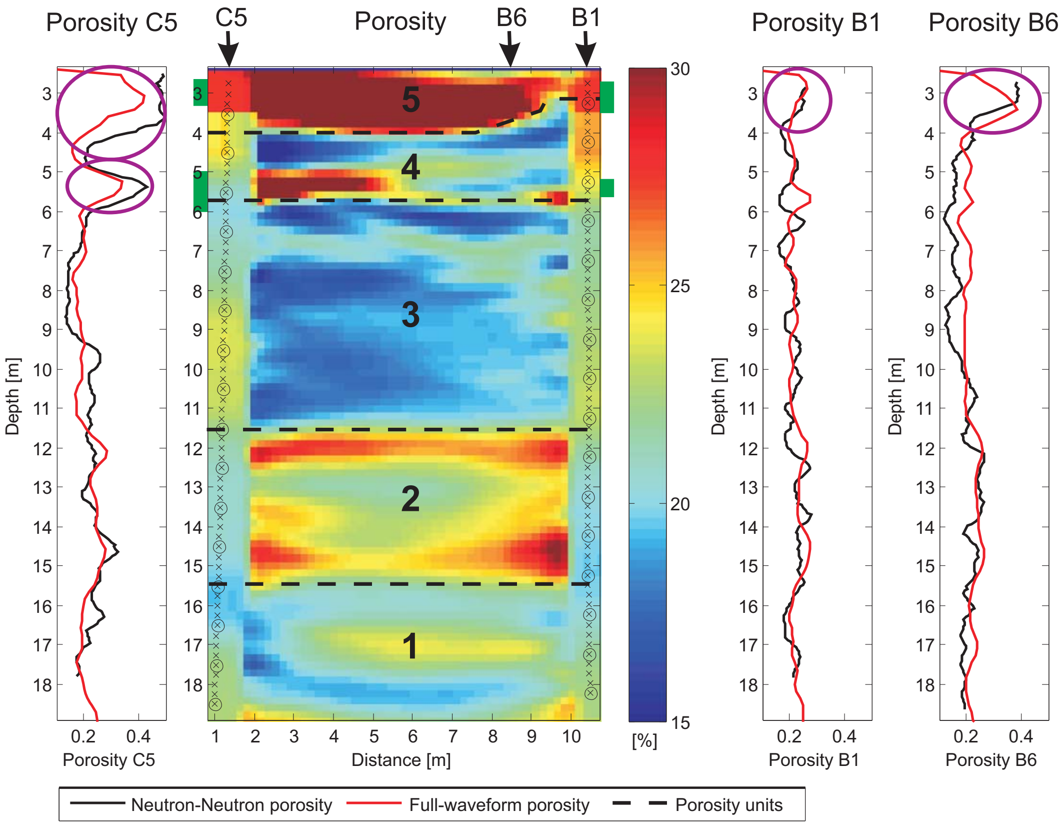

Figure 11. Converted full-waveform inversion porosity compared to Neutron-Neutron logging data (black graphs), acquired in boreholes C5, B6, and B1. The full-waveform inversion porosities close to the borehole locations are plotted as red graphs. The green boxes next to the image plot indicate the boundaries of the wave-guiding structures obtained from the amplitude analysis. The position of the boreholes corresponding to the image plot is marked by the black arrows. The numbers from 1 to 5 and the black dashed lines indicate the different porosity units. The purple circles indicate high-porosity zones in the logging data.

porosity (~20%), poorly sorted sand and gravel units to high-porosity sand units (~40%). Both layers are also visible in the logging data of well C5 (purple circles). In the image plot of the full-waveform porosities the five possible different hydrostratigraphic units are indicated by the black lines. The ray-based porosity shows only small variations in the porosity for the different units, whereas the full-waveform inversion resolved the porosity of each unit close to the values obtained by Neutron-Neutron data (see Table 2). The GPR full-waveform inversion obtained the depth of the boundary between Units 2 and 3 at approximately 11.5 m, whereas previous studies, e.g., of *Barrash and Clemo* [2002] based on Neutron-Neutron logging data indicated this boundary at 9 m depth.

The GPR profile (Figure 5) suggests that Unit 5 pinches out toward B1 and agrees with the full-waveform results that show clearly that Unit 5 is present between C5 and B6, and decreases the vertical extension between B6 and B1. The measured porosity logs confirm that Unit 5 is not present at B1. The identified sand lens between 5 and 6 m depth close to C5 was probably not clearly visible in the surface GPR data because of deconstructive interference between waves at the different unit boundaries. Since the model obtained with the full-waveform inversion explains the measured data very well and the Neutron-Neutron logs are more consistent with the extracted borehole data of the full-waveform, we consider these results as

Table 2. Porosity Estimates Based on Neutron-Neutron Logging Data (Mean Value of All Boreholes Located in the Center of the Test Site; See Table 1), Ray-Based and Full-Waveform Inversion Results for Each of the Hydrostratigraphic Units Indicated in Figure 11

Unit	Neutron-Neutron Mean Porosity (%)	Ray-Based Porosity (%)	Full-Waveform Porosity (%)
5	42.9	21.9	39.1
4	23.3	21.9	22.3
3	17.2	19.7	19.3
2	24.3	23.8	24.1
1	18.2	21.5	21.8
All	25.2	21.7	25.3

most reliable. Full-waveform inversion of the surface and crosshole GPR data will probably enable a high-resolution characterization of the unsaturated and saturated zone. However, the large velocity contrast between the saturated and unsaturated zone will require sophisticated full-waveform approaches [e.g., *Meles et al*., 2011] that enables the inversion of large-contrast medium properties.

5. Conclusions

We have investigated the complicated electromagnetic wave phenomena caused by the presence of a high-porosity (low-velocity) waveguide layers present between two boreholes. For transmitters located within a waveguide, at least 1 order of magnitude higher trace energy, a delayed travel time, and late arrival elongated wave trains are observed for receiver positions straddling along this zone. We showed that these elongated wave trains are formed by the trapping of the waves caused by total reflection beyond the critical angle. For receiver positions within the waveguide, a distinct minimum in the trace energy is present when the transmitter are located outside the waveguide because of the interference of the head waves from above and below the waveguide. These characteristic phenomena are used in an amplitude analysis that can directly be applied to identify high-contrast layers in the measured data.

We have performed several synthetic studies for high-porosity layers with different thicknesses, lateral extents, orientations (dipping), and model parameters. Our investigation of the influence of different permittivities and conductivities showed that in the presence of elongated wave trains, the waveguide is probably caused by a change in porosity rather than in clay content. For a continuous horizontal high-permittivity/porosity waveguide, similar wavefields with clear high-amplitude elongated wave trains and minima positions can be identified at similar depths of the semireciprocal setup. For a dipping high-porosity waveguide these features can be identified at different depths. If the thickness of the high-porosity layer is smaller than the sample spacing of the transmitter or receiver, the estimation of the boundaries is more challenging. When no transmitter is located in the waveguide and consequently no maxima occur, the minima position of the trace energy and the corresponding minima plateau can still be used to identify waveguides. For a terminated or spatially limited high-porosity waveguide layer that is connected to only one borehole, minima positions and increased amplitudes, and elongated wave trains can only be detected when receivers are within this borehole. For receivers present in the borehole that is not connected to the high-porosity layer, significant late arrival high-amplitude spreads are sensed in the data for the transmitter present at the waveguide depth, which is caused by the initial trapping of the waves within the waveguide followed by the release of the trapped wave energy when the waveguide is not present anymore. By analyzing the intensity and the spreading of the high-amplitude energy, a qualitative estimation can be made how far the high-porosity waveguide layer extends between the boreholes. For a high-porosity lens that was not connected to any of the boreholes, we found that the maxima positions can still be used to identify the lens as long the distance between the borehole and lens is not too big, but the detection of the lens boundaries is not possible.

We applied the extended amplitude analysis to an experimental data set from the BHRS, for which we detected two terminated wave-guiding structures close to the water table. For both waveguides, we observed significant spreading of late arrival high amplitudes indicating a limited lateral extent for both waveguides. We used the information gained from the amplitude analysis to improve the starting model for the full-waveform inversion and to obtain reliable inversion results. The final full-waveform inversion of these data showed two high-permittivity layers close to the water table whereas one layer was only present until the center of the domain (5–6 m depth) and the other almost for the entire distance of the boreholes (2.5–4 m depth). The obtained boundaries of the amplitude analysis were confirmed by the full-waveform inversion. Comparison with Neutron-Neutron logging data showed a good agreement with the converted full-waveform porosity. The lateral extent of the waveguide between 2.5 and 4 m depth was also confirmed in the Neutron-Neutron porosity logging data and indicated the origin of the waveguides as a change between sand and gravel in the aquifer. The extended amplitude analysis and crosshole GPR full-waveform inversion enables a detailed characterization of high-porosity waveguides of different extent, orientation and properties, and can be applied to a wide range of geological, hydrological, glacial, and periglacial studies to improve our ability to monitor and visualize important small-scale processes in the subsurface.

Acknowledgments
We thank Warren Barrash and the Department of Geosciences of the Boise State University for funding and providing the Neutron-Neutron log data for the SEG-AGU Hydrogeophysics workshop and this study. We acknowledge the support by the SFB/TR32 "Pattern in Soil-Vegetation-Atmosphere Systems: Monitoring, Modelling, and Data Assimilation" funded by the Deutsche Forschungsgemeinschaft (DFG), the Centre for High-Performance Scientific Computing in Terrestrial Systems (TerrSys), and the Juelich supercomputer center (JSC) for providing access to the JUROPA high-performance cluster where all our full-waveform inversions were calculated. We thank Steve Arcone, one anonymous reviewer, and Associate Editor Steven Moysey for their detailed reviews that significantly improved the paper.

References

al Hagrey, S. A., and C. Müller (2000), GPR study of pore water content and salinity in sand, *Geophys. Prospect.*, *48*(1), 63–85.

Alumbaugh, D., P. Y. Chang, L. Paprocki, J. R. Brainard, R. J. Glass, and C. A. Rautman (2002), Estimating moisture contents in the vadose zone using cross-borehole ground penetrating radar: A study of accuracy and repeatability, *Water Resour. Res.*, *38*(12), 1309, doi:10.1029/2001WR000754.

Arcone, S. A., P. R. Peapples, and L. B. Liu (2003), Propagation of a ground-penetrating radar (GPR) pulse in a thin-surface waveguide, *Geophysics*, *68*(6), 1922–1933.

Barrash, W., and T. Clemo (2002), Hierarchical geostatistics and multifacies systems: Boise Hydrogeophysical Research Site, Boise, Idaho, *Water Resour Res*, *38*(10), 1196, doi:10.1029/2002WR001436.

Barrash, W., and E. C. Reboulet (2004), Significance of porosity for stratigraphy and textural composition in subsurface, coarse fluvial deposits: Boise Hydrogeophysical Research Site, *Geol. Soc. Am. Bull.*, *116*(9–10), 1059–1073.

Barrash, W., T. Clemo, J. J. Fox, and T. C. Johnson (2006), Field, laboratory, and modeling investigation of the skin effect at wells with slotted casing, Boise Hydrogeophysical Research Site, *J. Hydrol.*, *326*(1–4), 181–198.

Binley, A., P. Winship, R. Middleton, M. Pokar, and J. West (2001), High-resolution characterization of vadose zone dynamics using cross-borehole radar, *Water Resour. Res.*, *37*(11), 2639–2652.

Bradford, J. (2010), Integrated hydrostratigraphic interpretation of 3D seismic-reflection and multifold pseudo-3D GPR data, in *Advances in Near-Surface Seismology and Ground-Penetrating Radar*, edited by J. H. B. Richard D. Miller, and K. Holliger, pp. 313–326, Soc. of Explor. Geophys., Tulsa, Okla.

Bradford, J. H., W. P. Clement, and W. Barrash (2009), Estimating porosity with ground-penetrating radar reflection tomography: A controlled 3-D experiment at the Boise Hydrogeophysical Research Site, *Water Resour. Res.*, *45*, W00D26, doi:10.1029/2008WR006960.

Clement, W. P., and W. Barrash (2006), Crosshole radar tomography in a fluvial aquifer near Boise, Idaho, *J. Environ. Eng. Geophys.*, *11*(3), 171–184.

Clement, W. P., M. D. Knoll, L. M. Liberty, P. R. Donaldson, P. Michaels, W. Barrash, and J. R. Pelton (1999), Geophysical surveys across the Boise Hydrogeophysical Research Site to determine geophysical parameters of a shallow, alluvial aquifer, paper presented at Symposium on the Application of Geophysics to Engineering and Environmental Problems, edited by M. H. Powers, L. Cramer, R. S. Bell, pp. 399–408, Environmental & Engineering Geophysical Society, Oakland, Calif.

Dafflon, B., J. Irving, and W. Barrash (2011), Inversion of multiple intersecting high-resolution crosshole GPR profiles for hydrological characterization at the Boise Hydrogeophysical Research Site, *J. Appl. Geophys.*, *73*(4), 305–314.

Davis, J. L., and A. P. Annan (1989), Ground-penetrating radar for high resolution mapping of soil and rock stratigraphy, *Geophys. Prospect.*, *37*, 531–551.

Doetsch, J., N. Linde, T. Vogt, A. Binley, and A. G. Green (2012), Imaging and quantifying salt-tracer transport in a riparian groundwater system by means of 3D ERT monitoring, *Geophysics*, *77*(5), B207–B218.

Ellefsen, K. J. (1999), Effects of layered sediments on the guided wave in crosswell radar data, *Geophysics*, *64*(6), 1698–1707.

Ernst, J. R., H. Maurer, A. G. Green, and K. Holliger (2007a), Full-waveform inversion of crosshole radar data based on 2-D finite-difference time-domain solutions of Maxwell's equations, *IEEE Trans. Geosci. Remote Sens.*, *45*(9), 2807–2828.

Ernst, J. R., A. G. Green, H. Maurer, and K. Holliger (2007b), Application of a new 2D time-domain full-waveform inversion scheme to crosshole radar data, *Geophysics*, *72*(5), J53–J64.

Franssens, G. R., P. E. Lagasse, and I. M. Mason (1985), Study of the leaking channel modes of in-seam exploration seismology by means of synthetic seismograms, *Geophysics*, *50*(3), 414–424.

Garambois, S., P. Senechal, and H. Perroud (2002), On the use of combined geophysical methods to assess water content and water conductivity of near-surface formations, *J. Hydrol.*, *259*(1–4), 32–48.

Greenhalgh, S. A., B. Zhou, D. R. Pant, and A. Green (2007), Numerical study of seismic scattering and waveguide excitation in faulted coal seams, *Geophys. Prospect.*, *55*(2), 185–198.

Hubbard, S. S., and Y. Rubin (2000), Hydrogeological parameter estimation using geophysical data: A review of selected techniques, *J. Contam. Hydrol.*, *45*(1–2), 3–34.

Hubbard, S. S., Y. Rubin, and E. Majer (1997), Ground-penetrating-radar-assisted saturation and permeability estimation in bimodal systems, *Water Resour. Res.*, *33*(5), 971–990.

Hubbard, S. S., J. S. Chen, J. Peterson, E. L. Majer, K. H. Williams, D. J. Swift, B. Mailloux, and Y. Rubin (2001), Hydrogeological characterization of the South Oyster Bacterial Transport Site using geophysical data, *Water Resour. Res.*, *37*(10), 2431–2456.

Irving, J., R. Knight, and K. Holliger (2009), Estimation of the lateral correlation structure of subsurface water content from surface-based ground-penetrating radar reflection images, *Water Resour. Res.*, *45*, W12404, doi:10.1029/2008WR007471.

Klotzsche, A., J. van der Kruk, G. A. Meles, J. Doetsch, H. Maurer, and N. Linde (2010), Full-waveform inversion of crosshole ground-penetrating radar data to characterize a gravel aquifer close to the Thur River, Switzerland, *Near Surface Geophys.*, *8*(6), 635–649.

Klotzsche, A., J. van der Kruk, G. Meles, and H. Vereecken (2012), Crosshole GPR full-waveform inversion of waveguides acting as preferential flow paths within aquifer systems, *Geophysics*, *77*(4), H57–H62.

Klotzsche, A., J. van der Kruk, N. Linde, J. Doetsch, and H. Vereecken (2013), 3-D characterization of high-permeability zones in a gravel aquifer using 2-D crosshole GPR full-waveform inversion and waveguide detection, *Geophys. J. Int.*, *195*, 932–944.

Koltermann, C. E., and S. M. Gorelick (1996), Heterogeneity in sedimentary deposits: A review of structure-imitating, process-imitating, and descriptive approaches, *Water Resour. Res.*, *32*(9), 2617–2658.

Kowalsky, M. B., S. Finsterle, J. Peterson, S. Hubbard, Y. Rubin, E. Majer, A. Ward, and G. Gee (2005), Estimation of field-scale soil hydraulic and dielectric parameters through joint inversion of GPR and hydrological data, *Water Resour. Res.*, *41*, W11425, doi:10.1029/2005WR004237.

Looms, M. C., K. H. Jensen, A. Binley, and L. Nielsen (2008), Monitoring unsaturated flow and transport using cross-borehole geophysical methods, *Vadose Zone J.*, *7*(1), 227–237.

Mangel, A. R., S. M. J. Moysey, J. C. Ryan, and J. A. Tarbutton (2012), Multi-offset ground-penetrating radar imaging of a lab-scale infiltration test, *Hydrol. Earth Syst. Sci.*, *16*, 4009–4022.

Meles, G., J. Van der Kruk, S. A. Greenhalgh, J. R. Ernst, H. Maurer, and A. G. Green (2010), A new vector waveform inversion algorithm for simultaneous updating of conductivity and permittivity parameters from combination crosshole/borehole-to-surface GPR data, *IEEE Trans. Geosci. Remote Sens.*, *48*(9), 3391–3407.

Meles, G., S. Greenhalgh, J. van der Kruk, A. Green, and H. Maurer (2011), Taming the non-linearity problem in GPR full-waveform inversion for high contrast media, *J. Appl. Geophys.*, *73*(2), 174–186.

Mwenifumbo, C. J., W. Barrash, and M. D. Knoll (2009), Capacitive conductivity logging and electrical stratigraphy in a high-resistivity aquifer, Boise Hydrogeophysical Research Site, *Geophysics*, *74*(3), E125–E133.

Oberröhrmann, M., A. Klotzsche, J. van der Kruk, and H. Vereecken (2013), Optimization of acquisition setup for cross-hole GPR fullwaveform inversion using checkerboard analysis, *Near Surface Geophys.*, *11*, 197–209.

Oldenborger, G. A., M. D. Knoll, P. S. Routh, and D. J. LaBrecque (2007), Time-lapse ERT monitoring of an injection/withdrawal experiment in a shallow unconfined aquilfer, *Geophysics*, *72*(4), F177–F187.

Straface, S., F. Chidichimo, E. Rizzo, M. Riva, W. Barrash, A. Revil, M. Cardiff, and A. Guadagnini (2011), Joint inversion of steady-state hydrologic and self-potential data for 3D hydraulic conductivity distribution at the Boise Hydrogeophysical Research Site, *J. Hydrol.*, *407*(1–4), 115–128.

Topp, G. C., J. L. Davis, and A. P. Annan (1980), Electromagnetic determination of soil water content: Measurements in coaxial transmission lines, *Water Resour. Res.*, *16*(3), 574–582, doi:10.1029/WR016i003p00574.

Tronicke, J., N. Blindow, R. Gross, and M. A. Lange (1999), Joint application of surface electrical resistivity- and GPR-measurements for groundwater exploration on the island of Spiekeroog—Northern Germany, *J. Hydrol.*, *223*(1–2), 44–53.

Tronicke, J., K. Holliger, W. Barrash, and M. D. Knoll (2004), Multivariate analysis of cross-hole georadar velocity and attenuation tomograms for aquifer zonation, *Water Resour. Res.*, *40*, W01519, doi:10.1029/2003WR002031.

van der Kruk, J., C. M. Steelman, A. L. Endres, and H. Vereecken (2009), Dispersion inversion of electromagnetic pulse propagation within freezing and thawing soil waveguides, *Geophys. Res. Lett.*, *36*, L18503, doi:10.1029/2009GL039581.

van der Kruk, J., R. W. Jacob, and H. Vereecken (2010), Properties of precipitation-induced multilayer surface waveguides derived from inversion of dispersive TE and TM GPR data, *Geophysics*, *75*(4), WA263–WA273.

Virieux, J., and S. Operto (2009), An overview of full-waveform inversion in exploration geophysics, *Geophysics*, *74*(6), WCC1–WCC26.

Winship, P., A. Binley, and D. Gomez (2006), Flow and transport in the unsaturated Sherwood Sandstone: characterization using cross-borehole geophysical methods, in *Fluid Flow and Solute Movement in Sandstones: The Onshore UK Permo-Triassic Red Bed Sequence*, edited by R. D. Barker and J. H. Tellam, pp. 219–231, Geological Society Special Publication, London, U. K., doi:10.1144/GSL.SP.2006.263.01.12.

Yang, X., A. Klotzsche, G. Meles, H. Vereecken, and J. van der Kruk (2003), Improvements in crosshole GPR full-waveform inversion and application on data measured at the Boise Hydrogeophysics Research Site, *J. Appl. Geophys*, *99*, 114–124, doi: 10.1016/j.jappgeo.2013.08.007.